Geophysical Journal International

Geophys. J. Int. (2014) **198,** 795–811
GJI Seismology

doi: 10.1093/gji/ggu072

Fundamental and higher two-dimensional resonance modes of an Alpine valley

Laura Ermert,[1] Valerio Poggi,[2] Jan Burjánek[2] and Donat Fäh[2]

[1] *Institute of Geophysics, ETH Zürich, CH-8092 Zürich, Switzerland. E-mail: laura.ermert@erdw.ethz.ch*
[2] *Swiss Seismological Service, ETH Zürich, CH-8092 Zürich, Switzerland*

Accepted 2014 February 21. Received 2014 February 13; in original form 2013 August 29

SUMMARY

We investigated the sequence of 2-D resonance modes of the sediment fill of Rhône Valley, Southern Swiss Alps, a strongly overdeepened, glacially carved basin with a sediment fill reaching a thickness of up to 900 m. From synchronous array recordings of ambient vibrations at six locations between Martigny and Sion we were able to identify several resonance modes, in particular, previously unmeasured higher modes. Data processing was performed with frequency domain decomposition of the cross-spectral density matrices of the recordings and with time-frequency dependent polarization analysis. 2-D finite element modal analysis was performed to support the interpretation of processing results and to investigate mode shapes at depth. In addition, several models of realistic bedrock geometries and velocity structures could be used to qualitatively assess the sensitivity of mode shape and particle motion dip angle to subsurface properties. The variability of modal characteristics due to subsurface properties makes an interpretation of the modes purely from surface observations challenging. We conclude that while a wealth of information on subsurface structure is contained in the modal characteristics, a careful strategy for their interpretation is needed to retrieve this information.

Key words: Site effects; Wave propagation.

1 INTRODUCTION

Besides constituting an important site effect in earthquake hazard analysis, resonances of seismic waves trapped in sedimentary bodies are commonly applied to study the properties of the resonating sediment. While often a 1-D model of sediment layers over bedrock half-space is sufficient to describe fundamental resonance frequencies and corresponding amplification levels, for deeply embanked valleys this approach was found inadequate (e.g. King & Tucker 1984; Bard & Bouchon 1985; Field *et al.* 1990; Guéguen *et al.* 2007). A deeper understanding of 2-D and 3-D basin resonance is therefore necessary both from a practical and a scientific point of view.

Although several studies have investigated 3-D resonance of simplified basins (e.g. Rial 1989), most studies have focused on 2-D models. This is because many locations where such resonances occur are indeed elongated and deeply incised valleys, so that along-valley variation of the sediment fill is small compared to the variation in the valley. Such valleys are commonly found in alpine regions. The importance of 2-D resonances in such settings has been investigated in a thorough numerical study by Bard & Bouchon (1985, hereafter abbreviated BB85). BB85 established a relation for the critical shape ratio $(h/l)_{\mathrm{crit}}$ of a basin, above which 2-D resonance and below which 1-D resonance and laterally propagating surface waves dominate. This critical shape ratio depends on sediment–bedrock velocity contrast and on incident wave type. It is lowest for *SV* modes and highest for *P* modes (i.e. *P* modes occur only in very deeply incised basins).

Subsequent modelling results from Moczo *et al.* (1996) indicated that 2-D resonance may occur also in valleys not fulfilling this condition, so that $(h/l)_{\mathrm{crit}}$ should be viewed more as an approximate indication than a strict criterion for the occurrence of 2-D resonance.

Different modes of basin resonance are characterized by their eigenfrequencies and mode shapes. BB85 have presented the modal characteristics of the three (*SH*, *SV*, *P*) fundamental modes. A schematic picture of these modes is shown in Fig. 1. In simplified terms, the sequence of modes of a sedimentary basin shows modes with a progressing number of nodes (locations where no motion occurs) at increasing frequencies. However, little is known about the sequence of modes occurring in a realistic basin.

Given their effects on ground motion, extensive theoretical studies on 2-D resonances exist already, including analytic and semi-analytic approaches (e.g. Trifunac 1971; Wirgin 1995; Yeh *et al.* 1998; Paolucci 1999) and a large number of numerical simulations (e.g. BB85, Fäh *et al.* 1994; Moczo *et al.* 1996; Steimen *et al.* 2003; Frischknecht & Wagner 2004; Roten *et al.* 2006; Roten *et al.*

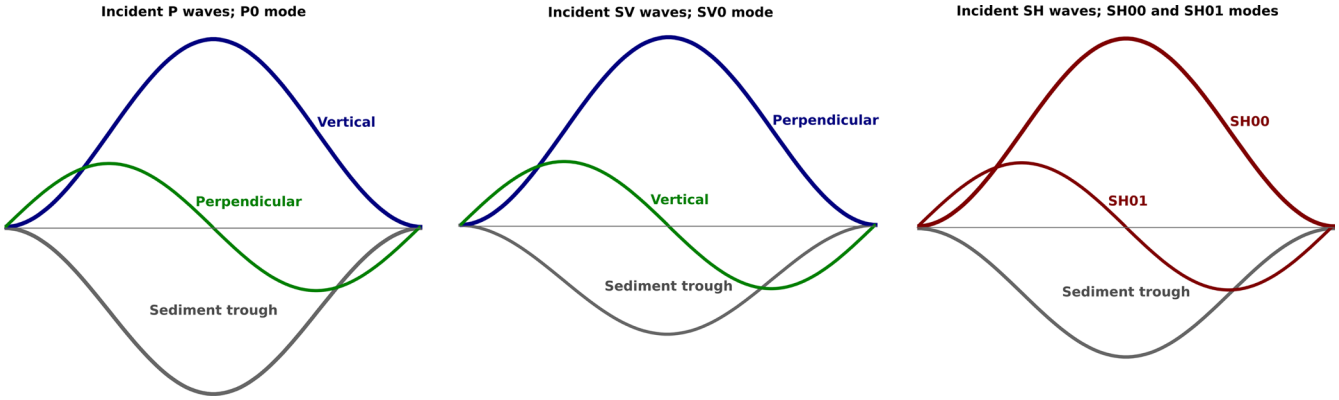

Figure 1. Schematic representation of the fundamental *P* and *SV* and the fundamental and first higher *SH* mode. Schematic mode shapes are shown by coloured curves. Sediment–bedrock interface is shown by grey line. Different depths of the sediment trough indicate different critical shape ratios for *P*, *SV* and *SH* modes. Note that *P* and *SV* mode each include horizontal and vertical motion. Modified from Steimen *et al.* (2003) and BB85.

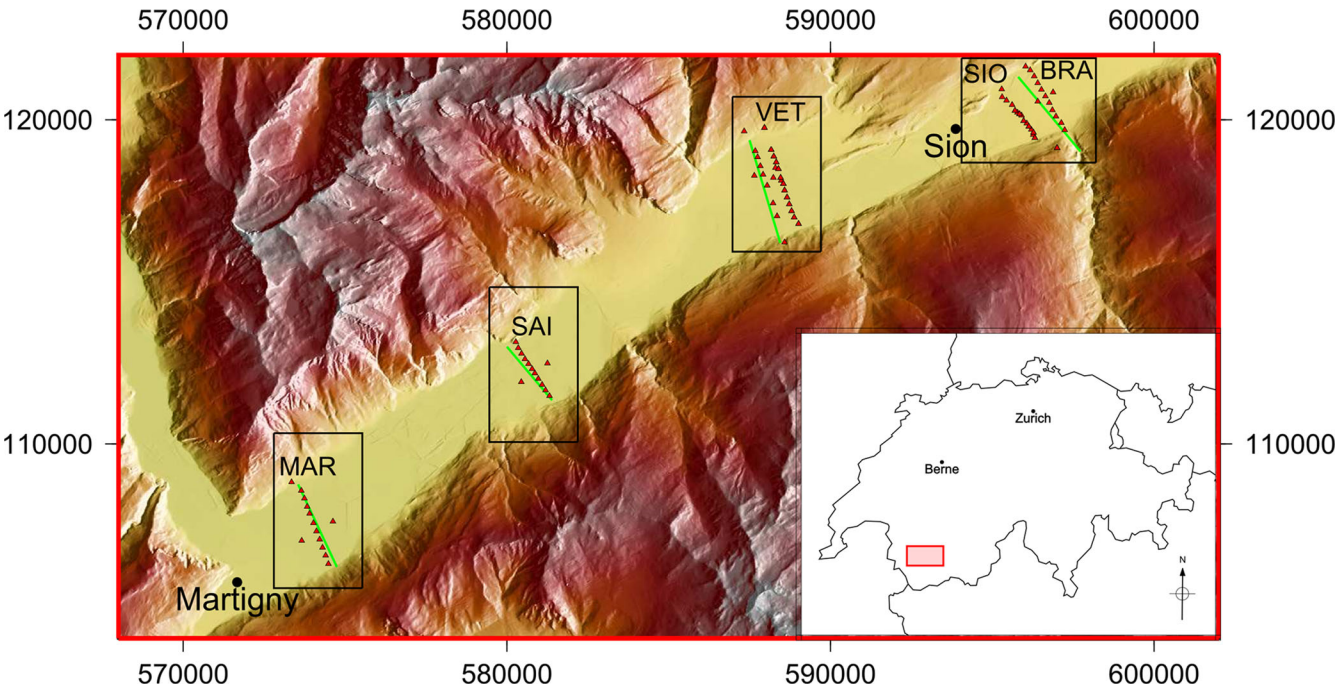

Figure 2. Geographic setting. Coordinates on map are Swiss national coordinates in metres. Array stations are shown by red triangles. Green lines indicate the location of the seismic profiles from Pfiffner *et al.* (1997).

2008; Havenith *et al.* 2009; Le Roux *et al.* 2012). Conversely, only a small number of studies include actual observations of the phenomenon. In particular, observational evidence has been suggested for a valley in Flushing Meadows, USA (Field *et al.* 1990), the Chusal valley, Tajikistan (King & Tucker 1984), the Grenoble basin (Guéguen *et al.* 2007) and the Romanche valley (Le Roux *et al.* 2012), both in the French Alps. A well-documented case of 2-D resonance is known from several studies performed in the Rhône valley, Swiss Alps (Steimen *et al.* 2003; Roten *et al.* 2006). Here, resonance frequencies obtained from synchronous array recordings of ambient vibrations were used as additional constraint in an inversion for sediment shear wave velocity (v_s) by Roten & Fäh (2007).

The goal of this study is to investigate the sequence of modes of a realistic basin. More insight on higher modes is to be gained. Besides, we aim to determine whether 2-D resonance frequencies, but also mode shapes, are suitable for inversion for subsurface structural characteristics (similar to, and adding upon the inversion conducted by Roten & Fäh 2007). Ambient vibration measurements from previous surveys in the Rhône valley and from two new synchronous array measurements at Sion (*cf.* map in Fig. 2) are analysed with two new data processing techniques, frequency domain decomposition (Brincker *et al.* 2001) and time-frequency dependent polarization analysis (Burjánek *et al.* 2012). Finite element simulations are presented in order to support observational results, and also to investigate sediment motion at depth. Observations and numerical results are compared in terms of eigenfrequencies and surface mode shapes. This comparison allows deducing the node number at depth from surficial observations. Particular attention is paid to the appearance of (1) modes with a node in vertical direction (inside the sediment fill), which could previously not be observed from measurements, and (2) the so-called breathing or P_0 mode, because this mode was predicted to occur in deeply embanked valleys by BB85, but also remained yet unobserved.

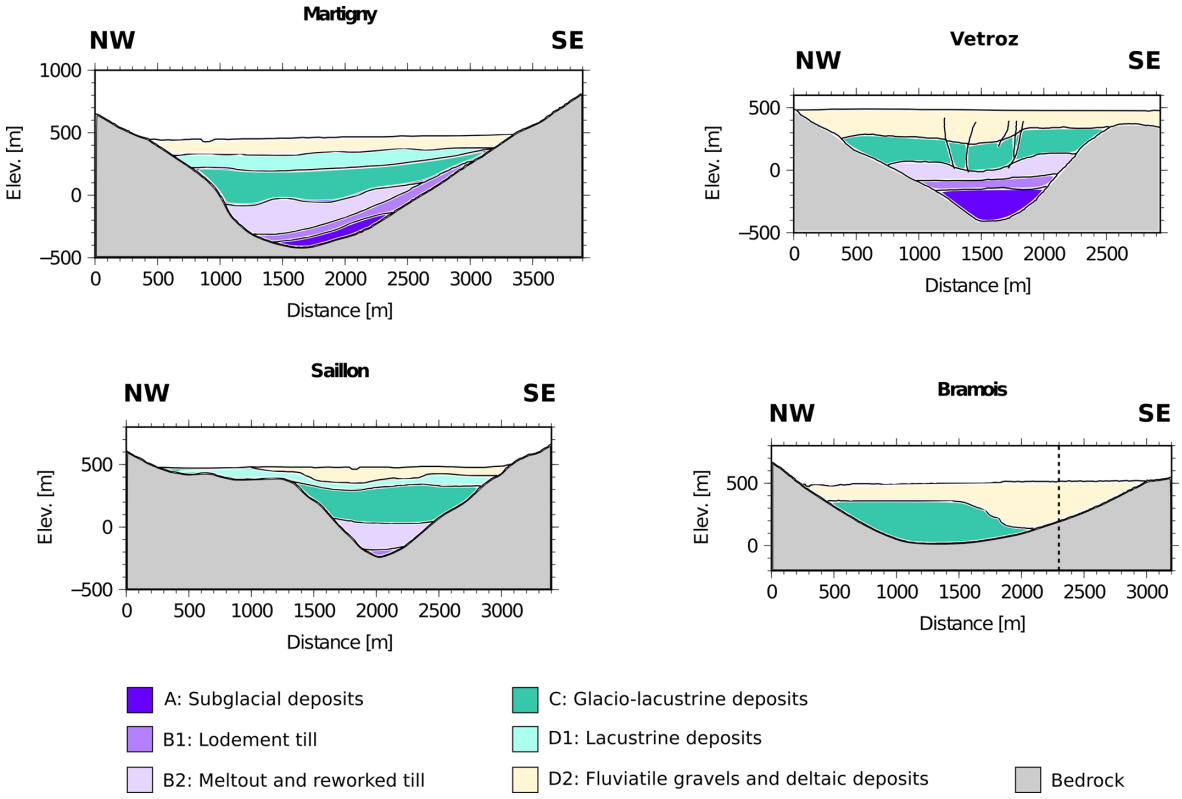

Figure 3. Geological interpretations of the sediment fill at four locations in Rhone Valley based on seismic reflection results. Modified from Pfiffner *et al.* (1997). The dashed line on Bramois profile shows the approximate location where the seismic line enters a tributary valley.

In addition, modelling results permit to qualitatively investigate the sensitivity of the fundamental *SH* and *SV* mode shapes to bedrock–sediment interface shape (which is referred to as valley shape in the following) and to velocity structure. The fundamental *SH* mode shape is directly compared to valley shape, while in the *SV* case the dip angle of particle motion can be used to assess perpendicular and vertical components conveniently in one quantity. The dip angle can be observed directly by time-frequency dependent polarization analysis of the recorded time-series (*cf.* chapter methods) from single stations. The question of sensitivity of the mode shapes is also approached by comparing them to results from reflection seismics (Pfiffner *et al.* 1997).

Different terminologies for describing 2-D resonance are found in literature. Here, we use the terminology introduced by Field (1996). The components of sediment motion due to resonance are denoted by axial or *SH* (the component along the valley axis), perpendicular (the component perpendicular to the valley axis) and vertical. Previous studies (BB85; Steimen *et al.* 2003; Roten *et al.* 2006) distinguish between modes excited by incident *P* and incident *SV* waves. In this study, we summarize them as *P–SV* modes since generally both include motion on perpendicular and vertical component; however, we denote the 'in-plane shear and in-plane bulk mode' described by BB85 as SV_0 and P_0, respectively.

2 GEOGRAPHICAL AND GEOLOGICAL SETTING

The Rhône valley, situated in the Southern Swiss Alps, is a glacially carved valley. Glacial and fluvial sediments reaching a thickness of up to 900 m overly different types of bedrock from crystalline basement to sedimentary rocks of the Helvetic nappes (Pfiffner *et al.* 1997).

A considerable amount of geophysical data on the lower part of the Rhône valley is available from previous studies, which makes this area an ideal site to investigate the sensitivity of 2-D resonances. In particular, four high-resolution seismic reflection profiles perpendicular to the valley axis at the locations shown in Fig. 2 were acquired during a Swiss national research project (NRP20, Pfiffner *et al.* 1997). Geological interpretations based on these profiles are shown in Fig. 3. At most of the investigated locations, the bedrock interface is deeply incised with resulting shape ratios well above the critical shape ratio. Only close to Sion (line Bramois) the shape ratio is relatively low (approximately critical). Concerning the location of the Bramois profile, it should be noted that the seismic line followed the Borgne tributary so that the SE end of the line is located more than 500 m up the tributary valley (Fig. 2). Thus, at Bramois, the southeasternmost part of the sediment fill represents the sediment fill of the tributary rather than the main valley. Glacio-lacustrine deposits of the main valley are therefore only found in the northwest part of the profile. Cross-sections at Martigny and Vétroz show strongly asymmetric shapes of the sediment–bedrock interface. Velocity and bedrock shape based on these profiles were used by Roten & Fäh (2007) as base for their v_s inversion study. Information from the profiles is used here together with results of this inversion in our finite element models.

3 PROCESSING METHODS AND DATA

Both single station and array ambient vibration records have been used in the past to measure 2-D resonance frequencies (Field *et al.*

1990; Steimen *et al.* 2003; Roten *et al.* 2006). Methods based on ambient vibration recordings are most suitable for regions of moderate seismicity, such as the Rhône valley, since array earthquake recordings require a long operation time of the instruments. Precise sources of ambient vibrations as well as the relative contributions of body and surface waves to the ambient wavefield are generally unknown (Bonnefoy-Claudet *et al.* 2006). Therefore, statistical approaches to processing are used. In this study, we implement frequency domain decomposition (FDD) (Brincker *et al.* 2001; Michel *et al.* 2010) and polarization analysis (PA) (Burjánek *et al.* 2012). Earlier studies (Steimen *et al.* 2003; Roten *et al.* 2006) used the reference station or standard spectral ratio method. This technique exploits spectral ratios of the array stations with respect to a reference station on bedrock in order to obtain apparent amplification of the sediment. The main disadvantage of this method is that it requires a reference station on bedrock, a suitable location for which cannot always be found.

3.1 Frequency domain decomposition (FDD)

The FDD method has proven useful for determining eigenmodes of civil engineering structures with ambient vibration excitation (Michel *et al.* 2010). The method is based on the spectral decomposition of the cross-power spectral density (PSD) matrix between all receivers of the array. Ideally, the source wavefield consists of Gaussian white noise and material behaviour is perfectly elastic. In this case, the eigenvalues of the cross-PSD matrices equal the auto-PSD functions of single degree of freedom systems representing the modes occurring at this frequency. Thus, the largest eigenvalue of the PSD matrix at all frequencies shows peaks at the resonance frequencies, as demonstrated by Brincker *et al.* (2001). The eigenvectors associated with these peak eigenvalues yield estimates of the corresponding mode shapes. Stacking of many realizations of the array cross-PSD matrix ensures minimization of uncorrelated noise (including sensor noise, short-time local ground vibrations, etc.).

Although the assumption of a perfect white noise source wavefield is clearly not fulfilled in our measurements (as for example a spectral peak due to oceanic microseisms is often observed), approximate results for the modal characteristics can still be obtained (Brincker *et al.* 2001). The FDD method can be applied profitably to three components, i.e. correlating all components recorded by the seismometer. Although we ran preliminary tests on this, we ultimately decided to enforce a 2-D modal analysis by analysing the P-SV and SH components separately. This simplified the modelling approach greatly; furthermore, it allowed us to directly link our interpretation to the description of 2-D modal sequences by BB85. Compared to the standard spectral ratios, the frequency domain decomposition has the advantages that no reference station is needed and that phase information is included in the mode shapes (e.g. upward/downward motion of SH01), so that nodes can be identified more reliably, which should allow to map more of the higher modes.

3.2 Polarization analysis (PA)

Results from FDD were compared to results obtained with time-frequency dependent PA (Burjánek *et al.* 2012). This method allows quick assessment of ground motion polarization at each station. It is expected that ground motion polarization reveals 2-D resonance, since resonance causes the ground to oscillate preferentially in the direction of the resonance mode, whereas generally ambient vibration, under the assumption of regularly distributed sources, is of random orientation. If close-to-linear motion with a consistent frequency and direction occurs frequently at several stations across a valley, it can indicate a resonance frequency. Spatial orientation of the motion with respect to the valley axis indicates additionally whether a *SH* or *P–SV* mode is observed. For a description of the PA procedure the reader is referred to Burjánek *et al.* (2010, 2012). The procedure is only briefly summarized in the following.

Time-frequency dependent polarization analysis is an extension of the complex polarization analysis procedure proposed by Vidale (1986). To investigate polarization in different frequency bands, each signal is first decomposed by continuous wavelet transform (CWT). The particle motion ellipse obtained from complex PA is fully described by strike (angle of the semi-major axis from North), dip (angle of the semi-major axis from the horizontal) and ellipticity P_e (ratio of semi-minor to semi-major axis).

As mentioned, strongly polarized motion is indicated by preferential occurrence of one orientation (φ, δ) and close-to-linear motion (low ellipticity). Histograms showing the frequency of occurrence of strike, dip and ellipticity over time are therefore constructed for each frequency band obtained in CWT. Histograms at all frequencies are then combined in polar plots for φ and δ and in a Cartesian plot for ellipticity. These plots allow convenient assessment of ground motion polarization across the array. An example for plots of strike and ellipticity is shown in Fig. 4.

Even though polarization analysis does not add further information that cannot be retrieved with FDD, it has one strong advantage over this method: given a sufficiently stable wave field, it can in principle be performed with a single receiver, whereas for FDD an array is needed. If consistent results are obtained from both methods, therefore, PA can be considered the method of choice if only one or few stations are available.

3.3 Data

For applying the FDD method, synchronous array measurements are needed. In addition to already available linear array recordings from the locations Martigny, Saillon, Vétroz and Bramois (Roten *et al.* 2006; Roten & Fäh 2007), two new synchronous array measurements were acquired near Sion (Fig. 2) during the night from August 9 to 10, 2012. A bedrock reference station is not necessary for the processing methods used here, but was used to retain the possibility to perform standard spectral ratios. About 170 min of ambient vibrations were recorded with a short linear array spanning half the valley width and about 315 min with a long array covering almost the entire valley width (Fig. 2). The short configuration with denser receiver spacing was intended to resolve higher mode shapes, assuming that mode shapes are more or less symmetric. Twelve 3-component seismometers (Lennartz 3D-5s) were employed for the measurement. Two recordings from each configuration had to be discarded due to low quality, resulting in usable array recordings of nine instruments in the basin, respectively.

Recordings are oriented east–north-vertical and had to be rotated around the vertical axis before FDD processing so that one horizontal component aligns with the valley axis and the other is perpendicular to the valley axis. For consistency, we defined the valley axis at each location as the line perpendicular to the respective array.

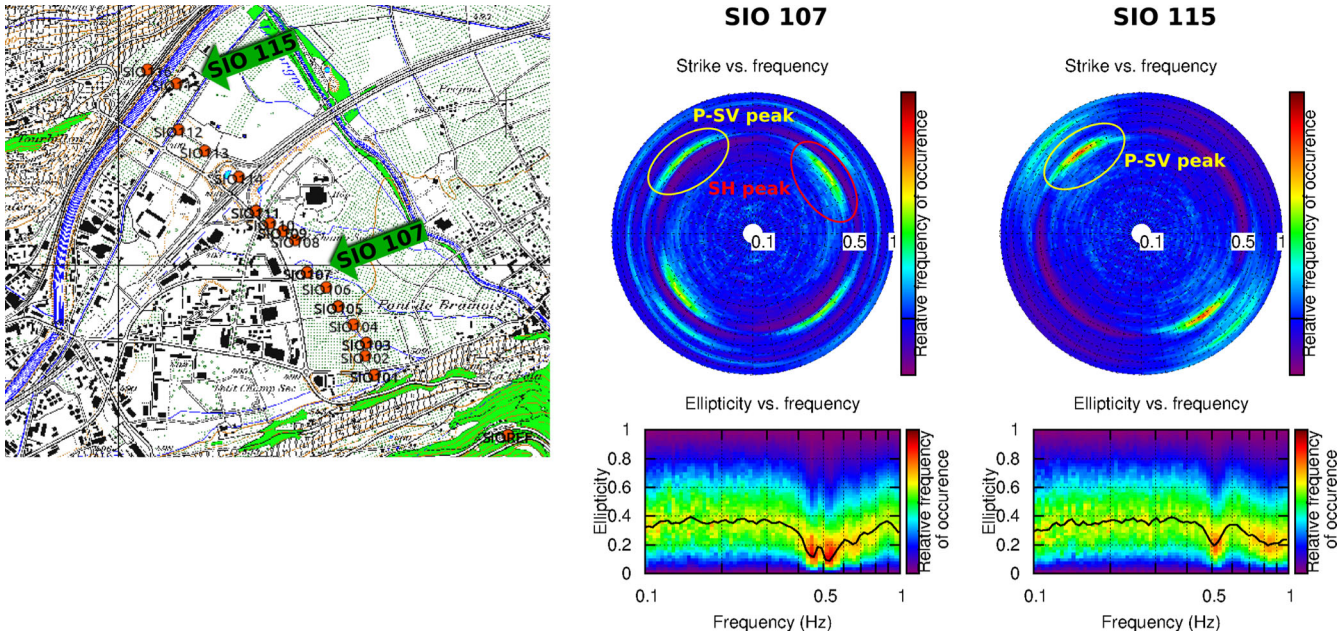

Figure 4. Polar plots showing the occurrence of strike orientation dependent on frequency (horizontal axis). Strike is 180°-periodic. Peaks of strike at an orientation parallel and perpendicular to the valley axis are interpreted as *SH* and *P–SV* resonance peaks, respectively.

4 RESULTS OF DATA PROCESSING

4.1 Incomplete mode separation

Fig. 5 shows the PSD curves of the axial and perpendicular component at Sion, first (short duration) measurement. These were obtained from the time-series by computing and averaging power spectral densities of 60 s Tukey windows with a 10 per cent taper and moving average smoothing applied in the frequency domain. A narrow smoothing window of a width of 0.004 Hz was applied so as not to broaden resonance peaks. The PSD curves contain several clear peaks, which were confirmed as resonance peaks by FDD (described below). They are indicated by arrows. Upon comparing the axial and perpendicular components shown in Fig. 5, it is evident that the separation into *SH* and *P–SV* modes is imperfect. A clear peak appears on the perpendicular component close to 0.5 Hz. A corresponding smaller peak is observed on the axial component. FDD enabled us to associate both peaks with the fundamental *SV* mode, since the axial component did not show any meaningful mode shape at this frequency. Thus, the peak was interpreted as fundamental *SV* mode and we discarded it from the set of *SH* modes. Such an overlap is expected, since the 2-D assumption is a clear simplification of the behaviour of the valley, and since sensor orientation, as well as rotation of traces, is not exact.

4.2 FDD results

From FDD processing, we obtained a large number of eigenvalue curves, such as those in Fig. 6(a). This example shows the axial component eigenvalues from both arrays at Sion. All peaks up to a frequency of 1 Hz were selected and the corresponding eigenvectors inspected. Wherever eigenvectors showed a mode shape that fit to our expectation drawing upon previous studies, frequency and mode shape were accordingly interpreted. As an example, the eigenvectors associated with the peaks at 0.46, 0.66, 0.78 and 0.98 Hz (marked by vertical solid black lines) are shown in panel (b). Orientation of the eigenvectors is SE–NW. They are normalized by their maximum absolute value. Due to their number of nodes, the eigenvectors shown here are interpreted as SH_{00}–SH_{03} mode

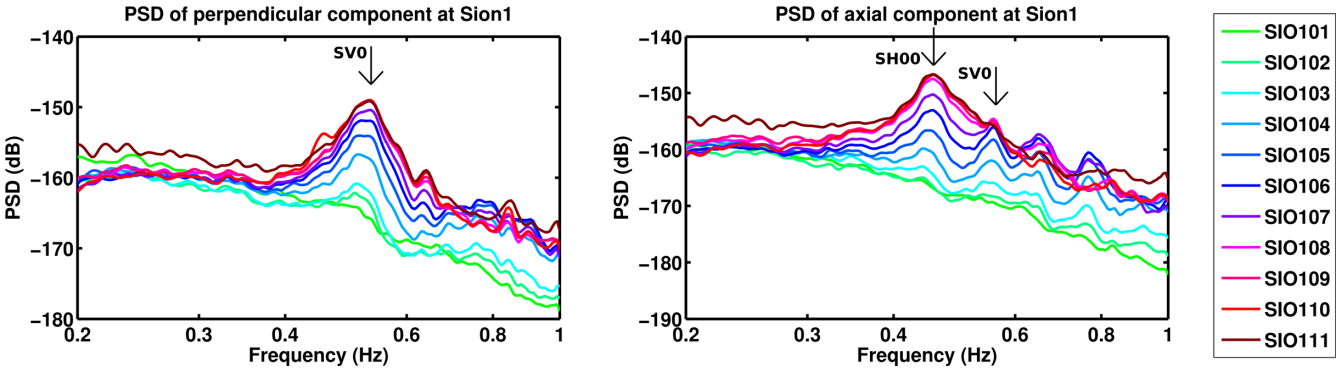

Figure 5. Power spectral densities of axial and perpendicular components of all array stations at Sion. The fundamental mode peaks can be seen at 0.42 Hz on the axial and at 0.52 Hz on the perpendicular component (marked by arrow here). The second peak on the axial component occurs around 0.55 Hz (also marked by arrow). We interpret it as being caused by the fundamental *SV* mode due to 3-D valley response or imperfect orientation of sensors.

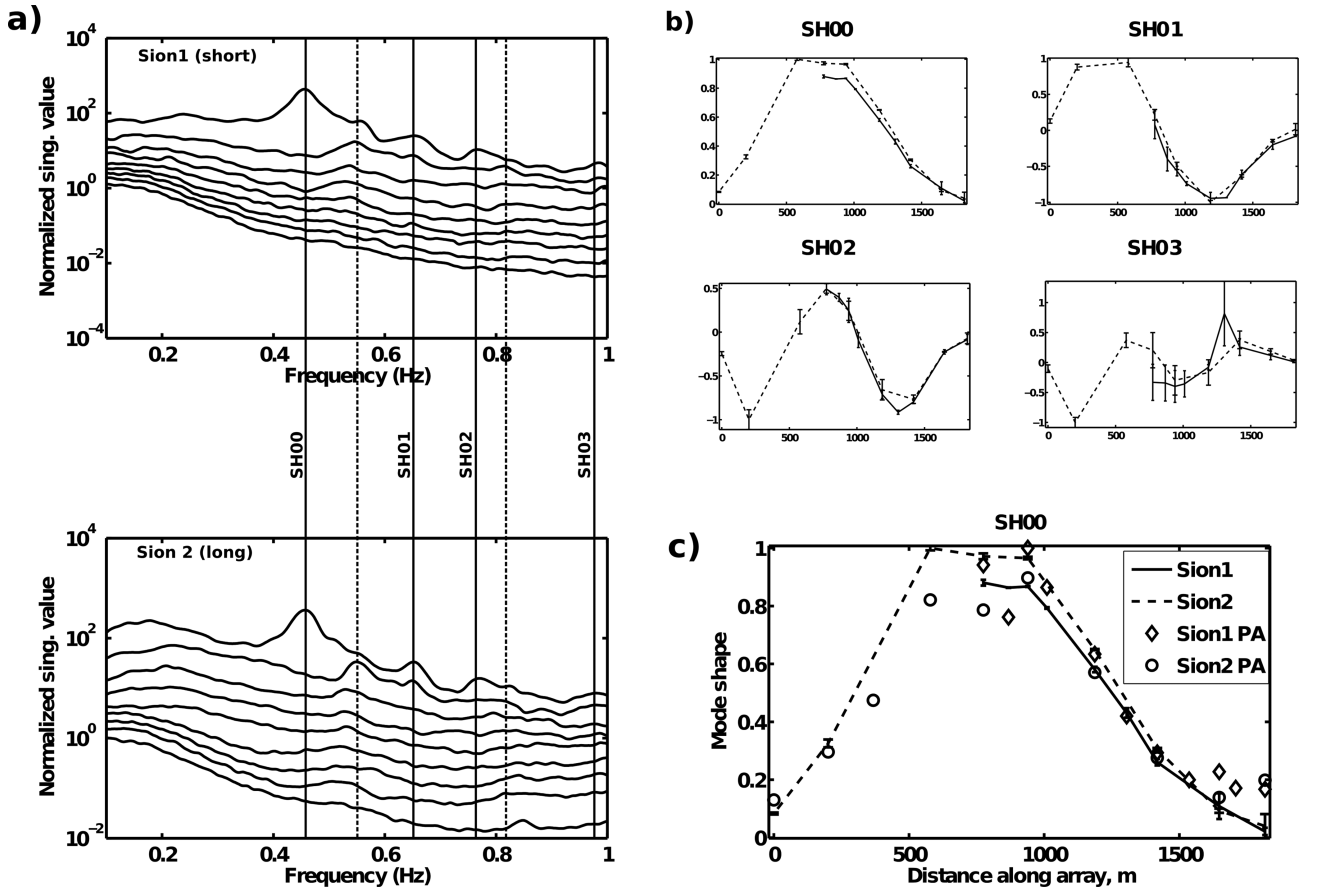

Figure 6. An example for the identification and interpretation of modal characteristics. The left plot shows eigenvalue curves obtained from the axial component of both arrays. Resonance frequencies are marked by vertical lines. Normalized eigenvectors are shown on the right with interpretation. These eigenvectors are the ones corresponding to the highest singular values marked by solid vertical lines on panel (a).

Table 1. All resonance frequencies identified with FDD and PA (italic numbers). Numbers in brackets denote frequencies identified by Roten & Fäh (2007) with the reference station method. Node numbers from surface observations (second column) determined the interpretation that is given on the right. Node number ?/1 for one of the *P–SV* modes indicates that this mode could only be observed on the vertical component.

Component	Horiz. node number	Martigny	Saillon	Vetroz	Sion (short)	Sion (long)	Bramois	Interpretation
Axial	0	0.3, *0.28* (*0.29*)	0.31, *0.31* (*0.32*)	0.35, *0.32* (*0.31*)	0.46, *0.47*	0.46, *0.47*	0.45, *0.45*	SH_{00}
Axial	1	0.38, *0.39* (*0.38*)	0.44, *0.42* (*0.43*)	0.43, *0.45* (*0.43*)	0.65, *0.66*	0.66, *0.66*	0.65	SH_{01}
Axial	2	0.44, *0.45* (*0.43*)	0.49, *0.50*	0.50, *0.55*	0.77, *0.77*	0.78, *0.78*	0.75	SH_{02}
Axial	3	0.51, *0.5*	0.58	0.58		0.98	0.99	SH_{03}
Axial	4	0.57	0.67					SH_{04}
Axial	5	0.63	0.76					SH_{05}
Perp./Vert.	0/1	0.33, *0.35* (*0.325*)	0.38, *0.38* (*0.37*)	0.39, *0.35* (*0.35*)	0.52, *0.52*	0.52, *0.52*	0.54, *0.55*	SV_0 of BB85
Perp./Vert.	1/2	0.45, *0.45*		0.51	0.81	0.81		
Perp./Vert.	?/1	0.55						
Perp./Vert.	2/3	0.64						
Perp./Vert.	3/4	0.69						
Perp./Vert.	4/5	0.78						
Perp./Vert.	Varying	0.84	0.84	0.84	0.84	0.84	0.84	

shapes. Interpretation in the *SH* case was possible without referring to numerical modal analysis, since the sequence of modes is simple. Vertical dashed lines in Fig. 6(a) mark peaks which were discarded since they are not associated with any meaningful mode shapes. Similar to the example presented here, FDD results from all locations were interpreted. All interpreted 2-D resonance frequencies are listed in Table 1. PA results (see below) are listed in italics. For comparison, results from Roten & Fäh (2007), obtained with the reference station method, are listed in brackets.

Using the FDD method, it was possible to identify and extract a larger number of modes than previously. Previous attempts to identify mode shapes were mostly limited to the fundamental *SH* and *SV* as well as the first higher *SH* mode, since spectral ratios with respect to bedrock yield clear peaks only for the lowest resonance modes, which are most amplified. Resonance frequencies observed on the axial component were directly interpreted as sequential *SH* modes (SH_{00}, SH_{01}, SH_{03}, . . .). Conversely, we did not assign interpretations to most *P–SV* modes prior to modelling. The *P–SV* case

contains both *P* and *SV* modes and shows a complicated sequence of modes due to the coupling of horizontal and vertical motion. Except for the fundamental *P* and the fundamental *SV* mode, there is no indication from previous studies (in particular BB85) as to the expected mode sequence. Therefore, we only assigned an interpretation to the SV_0 mode, for which a description is found in BB85 and which was previously observed (Roten *et al.* 2006). Modelling results shown below elucidated *P–SV* mode shapes in depth.

4.3 PA results

From *PA* processing, polar plots of strike, dip and a Cartesian plot of ellipticity for each station were obtained, from which frequency and orientation of strongly polarized motions were determined. First, peaks of strike were selected. If these occurred at several stations with consistent spatial orientation, either aligned with the valley axis or perpendicular to it, they were interpreted as resonance peaks. An example from Sion is shown in Fig. 4. An approximate value of the resonance frequencies was read from the plots, after which a simple grid search around this value was used to determine the frequency band containing the largest amount of polarized wavelets. This yielded the resonance frequencies listed in italic numbers in Table 1. Mode shapes of *SH* modes were reconstructed from PA by plotting the strike histogram value at the frequency and orientation associated with one mode against profile distance. The comparison with FDD result showed approximate agreement, as Fig. 6(c) illustrates. For the *P–SV* case, no mode shapes for the two components could be reconstructed from PA histograms due to the coupling of horizontal and vertical motion.

4.4 Comparison of observed mode shapes to bedrock interface shape

We compared mode shapes of the fundamental *SH* and the perpendicular part of the fundamental *SV* mode with the sediment–bedrock interface shape based on seismic lines (Pfiffner *et al.* 1997). The comparison is shown in Fig. 7. We placed the observed results with respect to the geographic position of the seismic lines as accurately as possible by considering endpoints of array and seismic lines (Pfiffner, personal communication, 2013). Since at Vétroz, a seismic model by Pfiffner *et al.* (1997) instead of the geological interpretation of the seismic lines is used, relative location of the array with respect to the valley shape is more uncertain than for the other profiles.

We observe that both *SH* and *SV* fundamental mode shapes resemble valley shape and cover almost the entire width of the valley at Martigny and Saillon. At Martigny, in particular, *SH* fundamental mode shape appears to mirror bedrock shape. On the other hand, the situation is more complicated at Vétroz. Mode shape is slightly narrower than valley shape. Moreover, it appears to map only the southern half of the valley shape. The bench-like feature at the south edge of the valley as well as the approximate slope of the interface are visible in the mode shape. However, the northern half of the mode shape terminates several 100 m before the valley edge. A particularity of the sediment fill at Vétroz is that seismic results show discontinuities interpreted by Pfiffner *et al.* (1997) as collapse structures of the sediment fill (Fig. 3). These are associated with lateral variation of several sedimentary strata, which might be linked to the focusing of the mode shape around the valley centre.

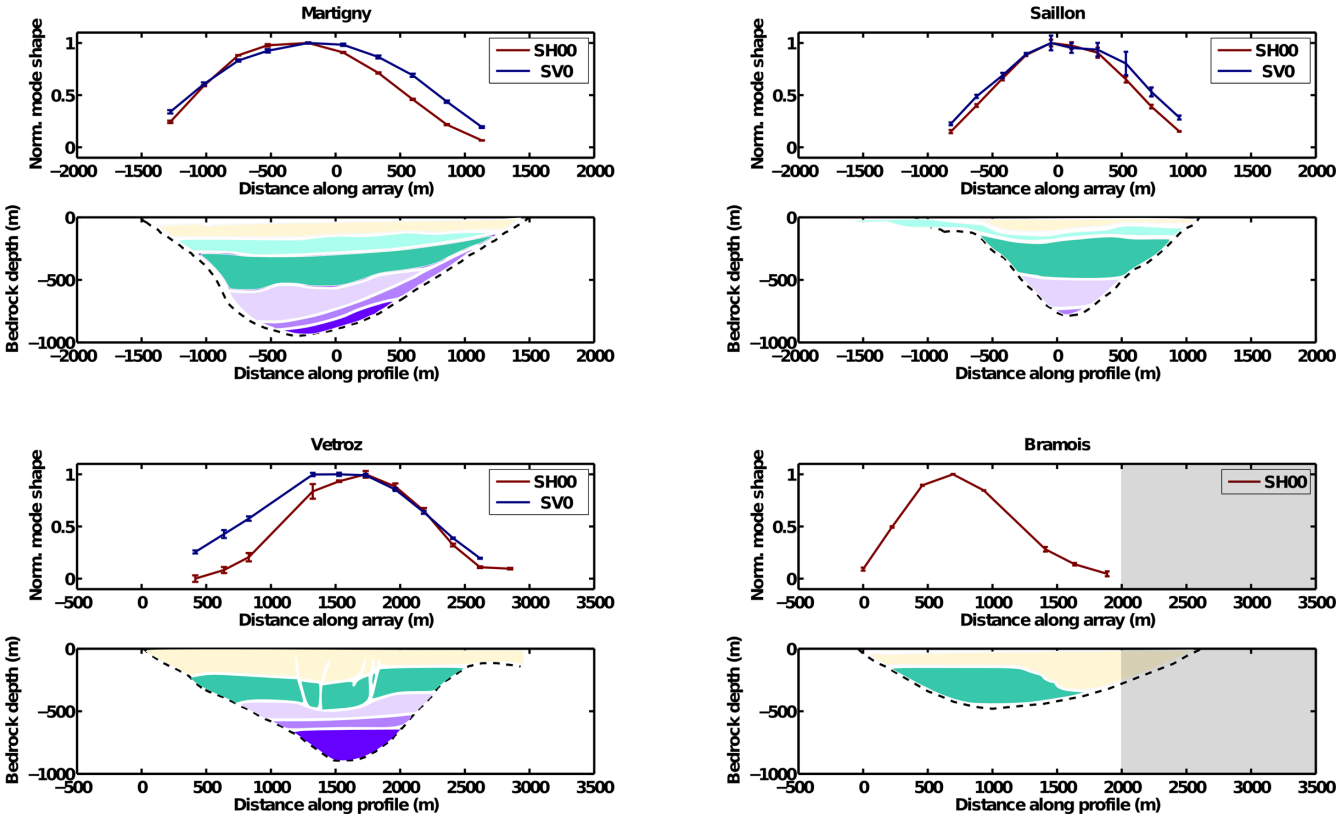

Figure 7. Comparison between the shape of the sediment–bedrock interface from seismic reflection studies (Pfiffner *et al.* 1997) and the mode shapes of the fundamental *SH* mode and the perpendicular component of the fundamental *SV* mode. Mode shapes are normalized to unity. Grey shaded area on Bramois profile shows approximate range of seismic line that is inside the tributary valley.

As pointed out above, the seismic line at Bramois enters a tributary valley approximately 800 m before the SE end of the line. Thus, the obtained mode shape covers approximately the extent of the main valley. A pronounced asymmetry is visible in mode shapes both from Sion (Fig. 6) and from Bramois (Fig. 7 lower right). Mode shapes have the peak on the northwest side of the valley. A possible explanation is that resonance is more strongly influenced by the glaciolacustrine deposits of unit C (Fig. 3), the extent of which coincides spatially with the peak of the mode shape.

5 FINITE ELEMENT MODELLING OF MODES

A detailed numerical study of 2-D resonance was performed in order to both interpret observations and understand the development of the higher modes in the valley. Two methods were adopted for modelling: (1) a semi-analytical approximate method based on Rayleigh's method; (2) fully numerical finite element modelling. The semi-analytic method allows for estimation of eigenfrequencies based on approximation of the mode shapes for simplified basin shapes. It was first applied to sediment resonance by Paolucci (1999). We used his REFORM code. Detailed description of the method can be found in Paolucci (1999), and in Roten & Fäh (2007) who applied REFORM as forward model in their inversion study for the shear wave velocity profile.

Resonance modes were modelled in 2-D with the modal analysis procedure of finite element package ANSYS (*ANSYS® Academic Research, Release 14.0*). The modes of the model structure are obtained directly from mass and stiffness matrices. No actual wave propagation is modelled. Due to several simplifications detailed below the approach here is less realistic than, for example, the finite difference models of Steimen *et al.* (2003) and Roten *et al.* (2006). However, it allows faster, more convenient and more extensive assessment of all sediment modes, even those with low energy content. All modes are evaluated regardless of the excitation level in the actual valley, and the approach is independent of any arbitrarily chosen sources.

PLANE183 elements with plane strain option were used to model the *P–SV* case, while FLUID29 elements were used for the *SH* case. Due to the analogue form taken on by the elastic wave equation simplified for *SH* waves and the acoustic equation, the latter can be used to model out-of-plane displacement in a sediment body in 2-D. This can be seen by comparing the acoustic equation in 2-D:

$$\frac{1}{\lambda_f}\ddot{p} = \frac{\partial}{\partial x}\left(\frac{1}{\rho_f}\frac{\partial p}{\partial x}\right) + \frac{\partial}{\partial z}\left(\frac{1}{\rho_f}\frac{\partial p}{\partial z}\right) \tag{1}$$

(e.g. Cerveny 2005), where λ_f is the first Lamé parameter of the fluid, ρ_f its density and p pressure, to the elastic wave equation simplified for 2-D *SH* waves

$$\rho_{el}\ddot{u}_y = \frac{\partial}{\partial x}\left(\mu\frac{\partial u_y}{\partial x}\right) + \frac{\partial}{\partial z}\left(\mu\frac{\partial u_y}{\partial z}\right) \tag{2}$$

(e.g. Aki & Richards 1980), where ρ_{el} is the density of the elastic material, μ is its shear modulus and u_y is out-of-plane displacement. Instead of solving the wave equation for displacement, one can obtain the same result by solving the acoustic equation for pressure, if the following substitutions are taken

$$\frac{1}{\lambda_f} = \rho_{el}, \tag{3}$$

$$v_f = v_s, \tag{4}$$

where v_s and v_f correspond to shear velocity of the elastic material and *P*-wave velocity in the fluid, respectively.

Meshing was done automatically in ANSYS, maximum element size was chosen manually. While for the homogeneous models a uniform edge length was used, for the layered models element edge length was varied from layer to layer in order to achieve adequate element sizes for thin layers. Maximum element edge length was 30 m in both cases. Considering modes with no more than 10 nodes in horizontal direction, that is, about five wavelengths inside the valley, with a 30 m element edge size, the mesh has more than 10 elements per wavelength.

A free surface and a perfectly rigid bedrock interface were assumed as boundary conditions. Resonance frequency is relatively insensitive to sediment–bedrock velocity contrast (BB85; Paolucci 1999). Only absolute amplification (which we do not consider) depends strongly on it. A rigid bedrock boundary ensures that results contain only modes of the sediment fill. It was implemented in the *P–SV* case by prescribing zero displacement (in both directions of motion) on the lines forming the basin bottom. In the *SH* case, zero pressure was prescribed in all nodes forming the basin bottom.

In both *P–SV* and *SH* case, 30 modes including mode shapes are extracted with a starting frequency of 0 Hz. The Block Lanczos solver chosen here includes a sequence check, which ensures completeness of the obtained mode set.

The modelling approach was compared to several other numerical and analytic approaches for the prediction of resonance frequencies and mode shapes of a basin, namely, the analytic solution for *SH* modes of a rectangle as found in BB85; the empiric formula by BB85 for basin *P–SV* fundamental modes and the analytic-based Rayleigh's approach implemented in REFORM. Excellent agreement was found between the homogeneous rectangle and the corresponding analytic solution for the *SH* case. Further tests revealed that the approach to model the *SH* case with acoustic elements in ANSYS cannot be extended to a layered medium. Thus, only homogeneous models were analysed in the *SH* case.

For the *P–SV* case, good agreement was found with the empirical formula of BB85. However, results from ANSYS and REFORM deviated strongly both in terms of resonance frequency (from about 40 per cent deviation for the fundamental mode to more than 80 per cent deviation for the second higher) and mode shape.

6 MODELLING RESULTS

We investigated the influence of different model parameters on modal shapes and eigenfrequencies. We studied effects related to different bedrock geometries, velocity structure of the sediment infill and Poisson ratio ν. The goal of this small parametric study was to support the interpretations of observations presented in Section 7. In particular, we focused on the addressing of the higher modes analysing the order of the eigenfrequencies and the relation of the mode shapes to the model geometry. In other words, the results of this section should serve as a guide for interpreting 2-D resonance observations, complementing the reference study BB85 with more realistic models.

6.1 Set-up of the parametric study

An overview of the models included in the parametric study is given in Table 2. Models 1–4 are intended for testing effects of different generic valley shapes and for comparison with analytical solution

Table 2. Properties of finite element models.

Nr.	Valley geometry	Layer nr.	Layer depth bottom (m)	Velocity model	V_p (m s^{-1})	V_s (m s^{-1})	Density (kg m^{-3})	Purpose of model
1	Box	1	Variable	Generic	1200	600	2000	Comparison to analytic solution, FD simulation and to empirical formula by BB85
2	Ellipse (Roten 06 elliptic valley)	1	770	Generic	1200	600	2000	Comparison to REFORM, comparison of valley shapes
3	Asymmetric (Roten 06 asymmetric valley)	1	770	Generic	1200	600	2000	Comparison to REFORM, comparison of valley shapes
4	Trapezoid	1	1000	Poisson ratio 0.2	1033	633	2000	Comparison of Poisson ratios
		1	1000	Poisson ratio 0.33	1193	601	2000	
		1	1000	Poisson ratio 0.45	1908	575	2000	
5	Vetroz 1 (NRP20)	1	890	Reflection seismic/inversion Martigny (mean)	1993	624	2000	Comparison of valley shapes
6	Bramois (NRP20)	1	480	Reflection seismic/inversion Martigny (mean)	1993	624	2000	Comparison of valley shapes
7	Martigny 1 (NRP20)	1	950	Reflection seismic/inversion Martigny (mean)	1993	624	2000	Comparison of valley shapes Comparison of velocity structures Comparison to observations
8	Martigny 2 (NRP20)	1	170	Reflection seismic/inversion Martigny (mean of upper and lower part)	1827	340	1900	Comparison of velocity structures
		2	950		2034	766	2000	Comparison to observations
9	Martigny 3 (NRP20)	1	170	Exaggerated velocity contrast	1000	200	1500	Comparison of velocity structures
		2	950		2000	1200	2300	Comparison to observations
10	Martigny 4 (NRP20)	1	3	Reflection seismic/Inversion Martigny	737	140	1500	Comparison of velocity structures
		2	26		1600	248	1600	Comparison to observations
		3	169		1930	374	2000	
		4	497		1970	705	2000	
		5	565		2300	816	2000	
		6	950		2050	822	2000	

and code REFORM; models 5–7 are intended for testing effects of different realistic valley shapes and models 7–10 for testing effects of the velocity structure as well as comparison to observations. In addition, model 4 was run with different Poisson ratios.

Material was assumed throughout to be linear elastic and isotropic. For the simplified valley shapes (box, and models compared to REFORM) several sets of generic material properties (see Table 2) were used. For the realistic valley geometries, a velocity model for Martigny from previous studies was employed: *S*-wave velocities are inversion results from Roten & Fäh (2007). *P*-wave velocities are taken from the NRP20 reflection seismic survey (Pfiffner *et al.* 1997). In addition, four versions of the realistic Martigny model were implemented to investigate sensitivity of the modal characteristics to velocity structure: In the first, velocities of all layers were averaged into a homogeneous model by using the traveltime-based average (*cf.* Roten *et al.* 2006). In the second, a simple two-layer model was obtained by traveltime averaging the upper three and the lower three layers, respectively. The third was the full six-layer model. In addition, a two-layer model with a strongly exaggerated velocity contrast (v_P contrast of 2 instead of approximately 1.1) between upper and lower layer was run. Only internally homogeneous and flat layers were considered to facilitate modelling procedure and interpretation of the modes and to permit comparison between ANSYS and REFORM.

6.2 Influence of valley shape

In a first step, we analysed the effect of bedrock geometry. The *SH* modal sequence of the simple box, ellipse and asymmetric models is shown in Fig. 8. The first row of plots shows the progression of axial modes with frequency as observed at the surface. Dashed lines are added for better readability. We found that especially for the *SH* case, such plots were excellent for assessing the mode sequence,

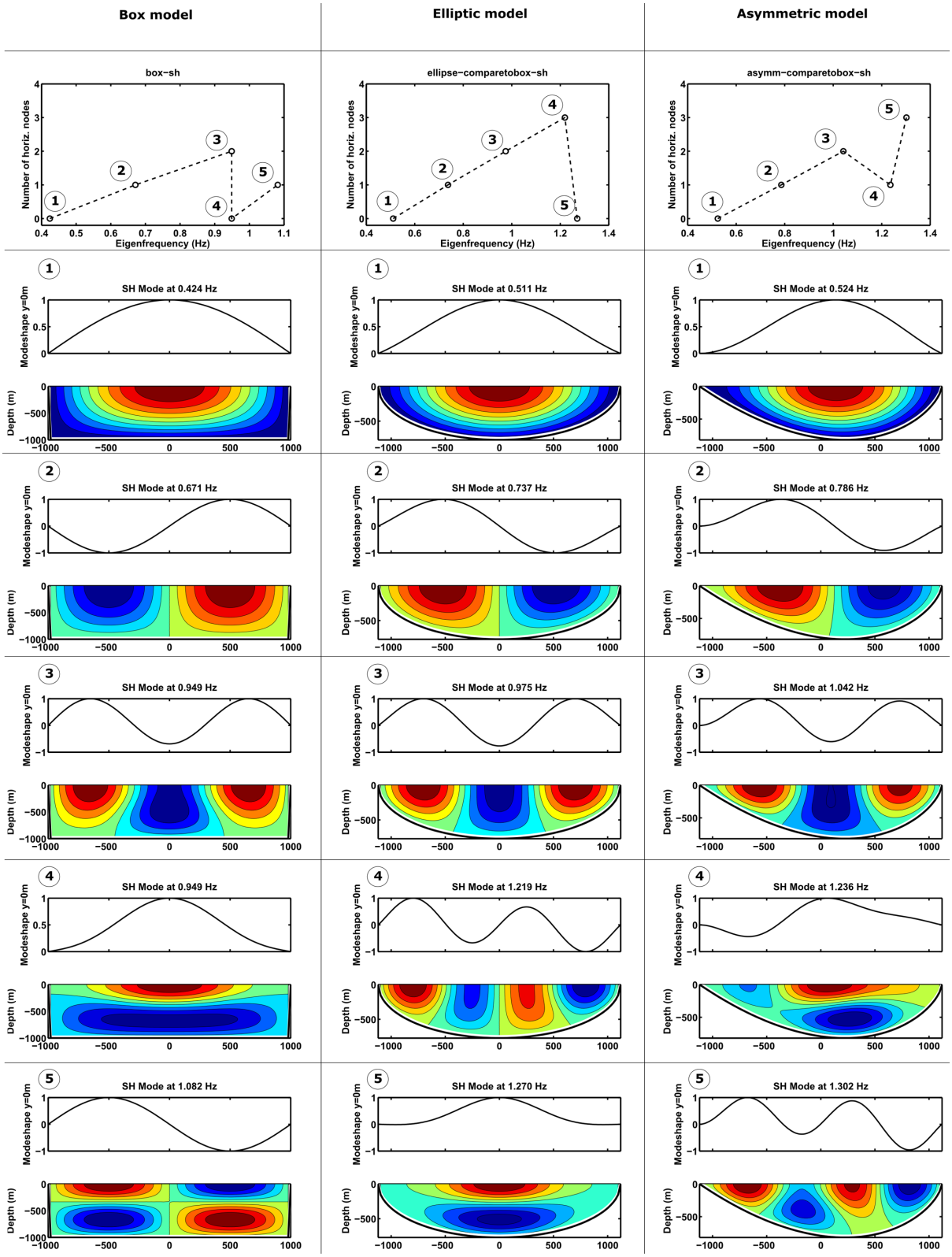

Figure 8. *SH* modes of three simplified models. Upper row of plots shows progression of modes (characterized by their horizontal node number) with frequency, which approximately follows a straight line for modes with the same number of vertical nodes. Line plots show surface mode shape (our observable). Contour plots show mode shapes in depth. Variations such as the one shown by the fourth mode of the asymmetric model (third column) illustrate that the sequence of node numbers can be strongly influenced by the valley shape.

since modes with the same number of nodes in vertical direction fall on an approximately straight line. This line is broken when an additional vertical node appears, as the horizontal node number drops in this case (as the sequence would read, e.g. $SH_{00} - SH_{01} - SH_{02} - SH_{10} \ldots$).

Concerning the mode shapes, two observations were made. First, the sequence of modes varies even with these simplified and relatively similar models, as for example, the SH_{10} mode appears later in the sequence in the elliptic model than in both others. Secondly, the valley shape induces variations of the mode sequence, as for example, the SH_{10} mode is replaced by an SH_{11} mode in the asymmetric model (fourth mode). Thus, not every node index occurs in each direction but modes may be left out.

Besides these simplified models, three different realistic valley shapes (Martigny, Vétroz, Bramois) were compared in order to qualitatively assess sensitivity of the *SH* fundamental mode shape. This sensitivity is indicated in our models by asymmetric valley shapes producing asymmetric mode shapes. Comparison of the location of peak in the mode shape with the valley centre shows that for each model the location of the maximum amplitude is shifted towards the side where the sediment deposit is deepest. However, the shift from the valley centre is subtle with approximately 200 m at Bramois and about 100 m at the other locations, corresponding to less than 10 per cent of the entire valley width in each case.

6.3 Effect of Poisson ratio on *P–SV* modes

In a second step, we tested the effect of two Poisson ratios used in the sensitivity study of BB85 (0.33 and 0.45) and one additional low Poisson ratio (0.2) on the modal sequence of a trapezoidal-shaped valley. By comparing resonance frequencies, we found the effect of the Poisson ratio on *SV* fundamental frequency is indeed very small, as reported by BB85. *SV* fundamental frequency varies by roughly 2 per cent. However, Poisson ratio does influence the *P* fundamental frequency, which varies by roughly 23 per cent. Consequently, the sequence of modes ordered by frequency changes. This is illustrated in Fig. 9.

Moreover, we observed that at high Poisson ratio, the P_0 mode does not appear (*cf.* Fig. 9). Instead, a mode of similar shape but with two nodes on the vertical component is observed. This demonstrates again that a one-by-one progression of node numbers cannot be expected. A detailed assessment is therefore necessary to interpret surface observations, which for the *P–SV* case of Martigny is presented in Section 7 (Synthesis).

6.4 Effects of the layered medium on *P–SV* modes

In a third step, we compared the influence of a varying number of flat sediment layers with different seismic velocities on the modal sequence. This was done only for *P–SV* modes due to the above-mentioned modelling constraints (*SH* case with acoustic elements in ANSYS could not be extended to a layered medium). An example of the three lowest modes of models Mar (Martigny) 1, Mar 3 and Mar 4 is shown in Fig. 10. The homogeneous model (left column) develops mode shapes affecting the entire valley fill. In contrast, the model with a high velocity contrast between lower and upper layer (middle column) shows modes that are clearly focused within the upper layer. Indeed, all first five modes of this model affect the upper layer only, which is illustrated by the one-by-one progression of node numbers shown in the upper plot. Comparison of surface mode shapes shows that these are symmetric in the case of the two-layer model, while strong asymmetries due to the valley shape can be observed in the homogeneous model. The realistic six-layer model shows intermediate behaviour. Although most displacement is focused in the upper three layers, the lower layers are also influencing the mode shapes. The sequence of modes, for the modes shown here, is similar to the homogeneous model. A smaller amount of asymmetry due to bedrock shape than in the homogeneous model is visible. The comparison between the models with different velocity structures evidence the sensitivity of *P–SV* surface mode shapes—and therefore related dip angles—to velocity structure.

6.5 Observations on the dip angle of SV_0

Finally, dip angles of the SV_0 mode were modelled to determine whether they carry meaningful information on the subsurface. Sensitivity of the SV_0 dip angle to both velocity structure and valley shape is presented in Fig. 11. Comparison of different valley shapes indicates that the maximal values of dip angle correlate spatially with the steepest parts of the bedrock interface. Also, the effect of the small bench-like feature in the Vétroz model is visible in the dip angle curve.

As indicated above, dip angle is also sensitive to the velocity structure of the sediment layers. The sensitivity to bedrock shape decreases with the introduction of a layered structure compared to a homogeneous velocity profile. Dip angles of the layered models are found to be more symmetric showing smaller variations.

Dip angle curves from the four models with different velocity structure show a common zero crossing and similar values at the valley edges. This suggests that zero crossing and dip angle at the valley edge are not sensitive to velocity structure, but rather related to valley shape.

7 SYNTHESIS OF MODELLED AND OBSERVED RESONANCE

The foremost aim of finite element modal analysis was to support the interpretation of observed modes, especially by determining the sequence of modes as characterized by node numbers in horizontal and vertical direction. As was discussed earlier, the curves of node number versus eigenfrequency were found useful in the assessment of the *SH* mode sequence. Such a curve for the observed axial modes is shown in Fig. 12. All node numbers identified from FDD and plotted with respect to corresponding eigenfrequencies fall on approximately straight lines. Thus, although a realistic layered model was not constructed for the *SH* case, modelling supports our interpretation that all of these measured modes belong to the SH_{0x} mode family. Moreover, the curves demonstrate that two distinct resonance behaviours exist in the southeast part of the studied area (locations Martigny, Saillon, Vétroz) as compared to the northwest part (locations Sion, Bramois).

A further example of how the modal analysis procedure complements observations is shown for Martigny. At this location most resonance frequencies were observed and the most detailed model was constructed. Table 3 lists observed and modelled modes. In the *SH* case we had to deal with the limitation of the homogeneous model.

In the *P-SV* case, a model equivalent of every observed mode can be found in the six-layer model, while not every modelled mode is actually observed. Surface mode shape was used as criterion to assign modelled to observed modes (Table 3). It was found that the mode shapes of the six-layer model Mar 4 generally fit best

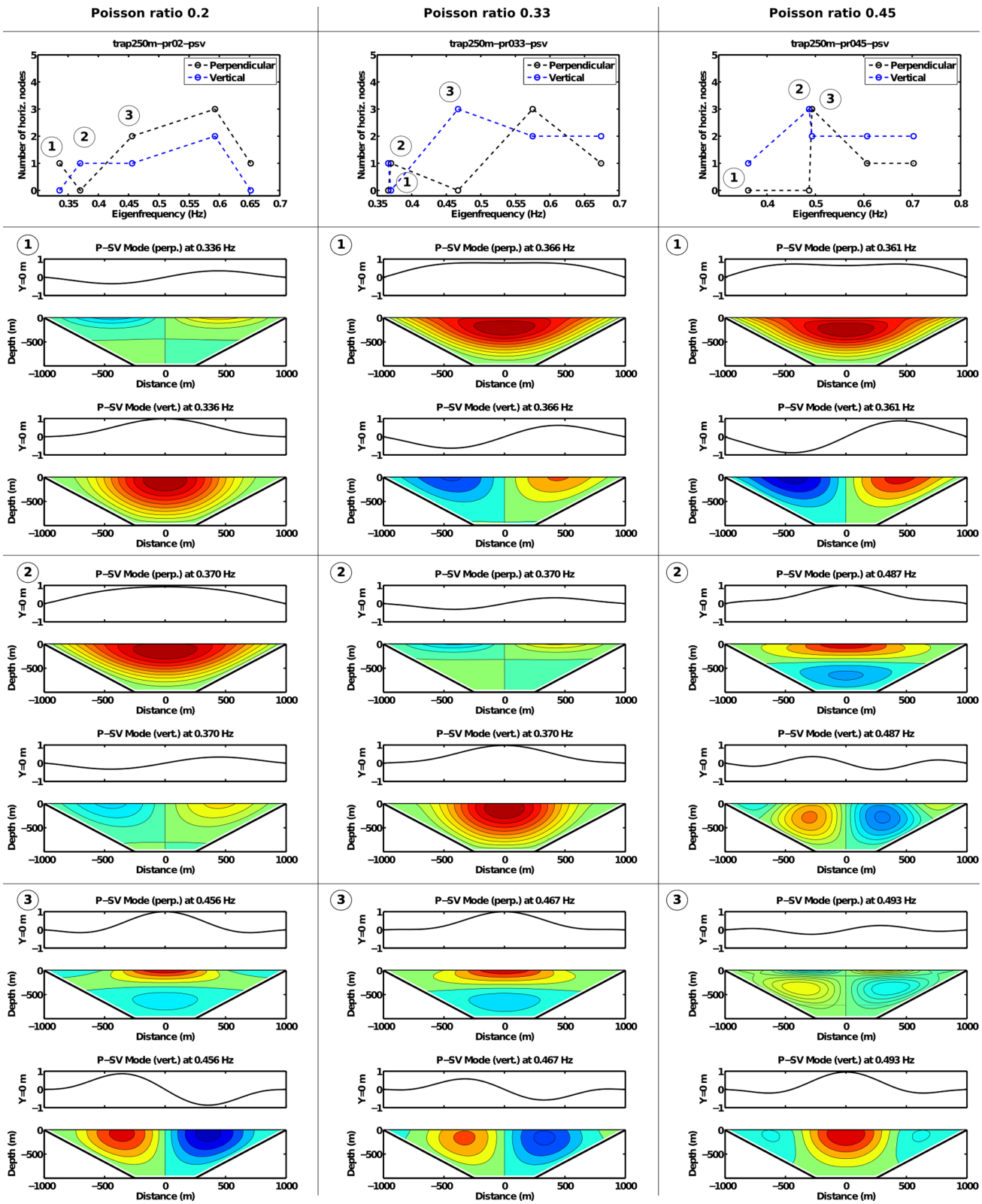

Figure 9. *P–SV* modes of models with three different Poisson ratios. Again, mode sequence, surface mode shapes and contour plots of mode shapes at depth are shown. Mode sequence depends on Poisson ratio. Moreover, the P_0 mode is not observed in the high-Poisson-ratio model (right column).

with the observed mode shapes. With the comparison that results from assigning observed modes to modelled ones based on their horizontal node numbers (observed at the surface), frequencies fit well with deviations of less than 10 per cent. Moreover, mode shapes show excellent agreement on certain details. Four examples are shown in Fig. 13. The broad shape of the fundamental mode is reproduced by the model. Note that on the observed mode shape, the edges are cut off since the array does not reach the very edge of the

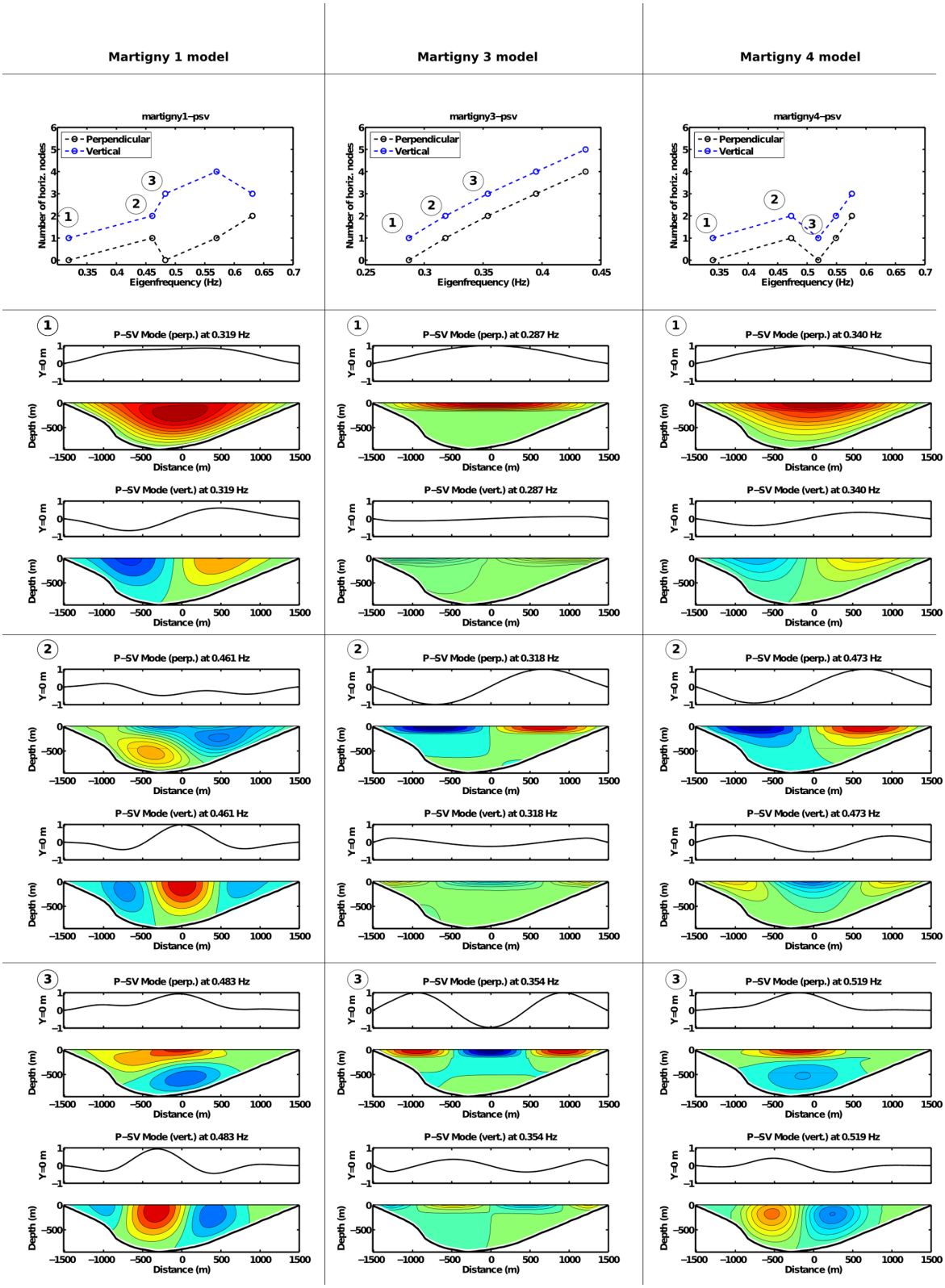

Figure 10. Lowest three *P–SV* modes of Martigny models. Sequence of modes, surface mode shapes and contour plots of mode shapes in depth are shown. Left column shows the homogeneous model, which has the same average velocity as the six-layer model shown in right column. Middle column shows a two-layer model with enhanced velocity contrast for comparison.

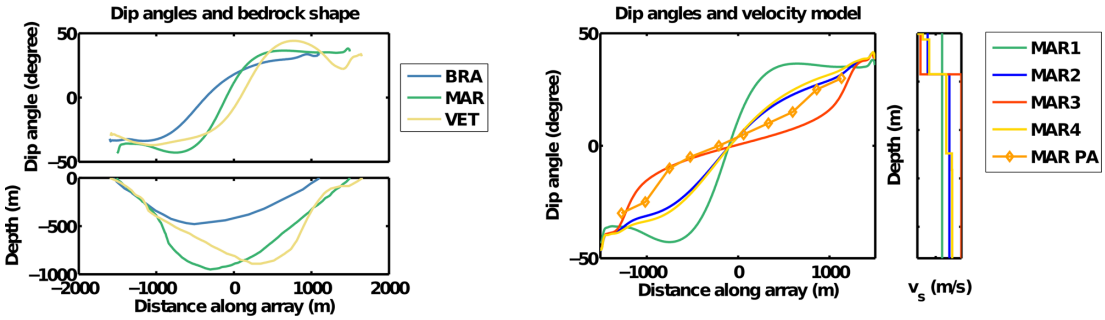

Figure 11. Dip angles for different valley shapes (left) and for different velocity models of the Martigny valley cross-section (right) also including observed dip angles from polarization analysis.

basin. Moreover, realistic mode shapes may extend into the bedrock. The model matches relative maximum amplitudes of perpendicular and vertical component in a qualitative way, although on close comparison, observed vertical amplitudes are smaller than expected from the model. When considering the perpendicular component of the mode at 0.662 Hz (lower right), the bulges in the valley centre are smaller compared to those at the edges. This can be observed also in the modelled mode shape. Such details are not reproduced by the homogeneous model Mar 1.

A further goal approached by modelling was to determine where in the modal sequence the first modes with nodes in vertical direction and the P_0 'breathing' mode appear. For the *P–SV* case, homogeneous and layered model provide slightly different frequencies: For the homogeneous model the first mode with a node in vertical direction occurs at about 0.48 Hz and for the six-layer model at 0.52 Hz. One observed mode may be linked to the latter. This mode is shown in Fig. 13, upper right panel. A corresponding observational mode shape could only be identified by processing the vertical component separately, as combined processing of perpendicular and vertical component resulted in inconclusive shapes with high uncertainties. Both modelled and observed mode shapes are narrower than the vertical component of the fundamental mode, distinguishing this mode from SV_0.

The P_0 mode in the strict sense does not occur in the six-layer model. As in the high-Poisson-ratio model in Fig. 9, only a similar mode with two horizontal nodes on the vertical component is modelled. FDD results were scanned carefully for a mode close to this frequency, but none could be found. Thus, the P_0 mode could not be observed.

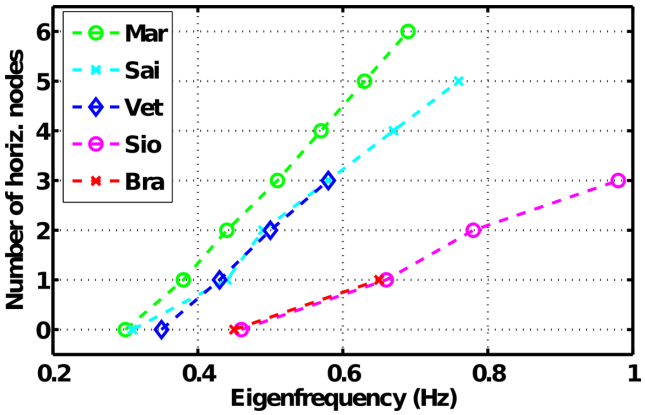

Figure 12. Progression of node numbers with frequency for observed *SH* modes at all locations. Node number is the number of zero crossings of the mode shape on the surface, as it was observed with FDD. The comparison to similar curves obtained from numerical modal analysis suggests that all the observed modes fall into the SH0x family. Moreover, one can see two distinct behaviours at Sion/Bramois on one hand (slow progression of node number with frequency) and the locations in the lower part of the valley on the other hand (steep progression of node number).

A comparison of modelled and observed dip angles (at location Martigny) can be found in Fig. 11 (right panel). Dip angles were read

Table 3. Comparison of modelled and observed modes for cross-section Martigny.

Interpretation	Observed frequency (Hz)	Observed horiz. node number(s) (in *P–SV* case perp./vert. component)	Model frequency (Hz)	Modelled vertical and horizontal node number(s)
SH_{00}	0.30	0	0.25	00
SH_{01}	0.38	1	0.37	01
SH_{02}	0.44	2	0.48	02
SH_{11}	Not observed	Not observed	0.56	11
SH_{04}	0.51	3	0.60	13
SH_{05}	0.57	4		
SV_0	0.33	0/1	0.34	00/01
	0.45	1/2	0.47	11/12
	0.55	Not observed/1	0.52	10/01
	Not observed	Not observed	0.55	11/02
	0.64	2/3	0.58	12/13
	0.69	3/4	0.66	13/14
	Not observed	Not observed	0.68	21/04
	Not observed	Not observed	0.68	13/16
	0.78	4/5	0.75	14/15

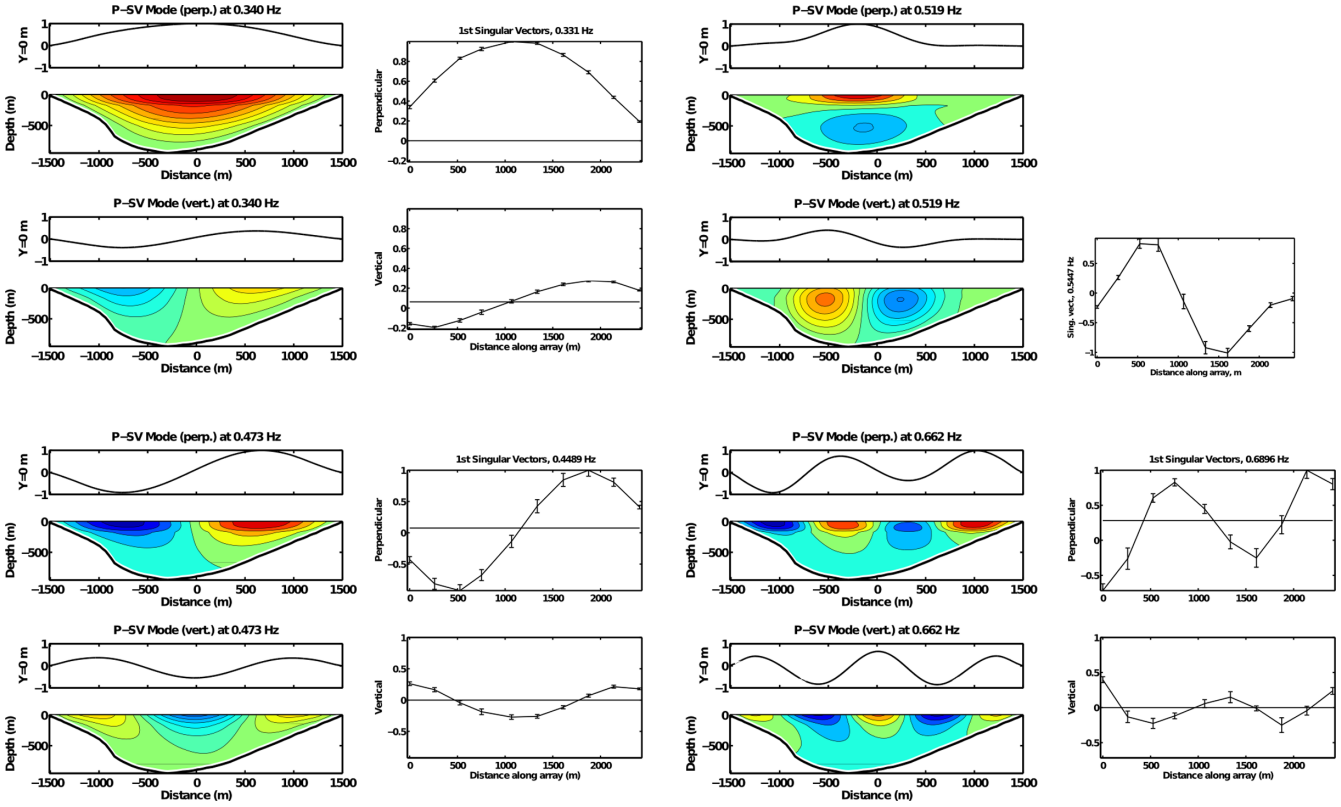

Figure 13. Comparison of observed to modelled *P–SV* mode shapes for location Martigny.

to the nearest 5° step from polar plots of dip obtained with PA. The comparison shows that zero crossing and edge value of the observed dip correspond closely to the modelled ones. The zero crossing is insensitive to changes in velocity structure, but is sensitive to valley shape. The fit obtained here indicates therefore that valley shape is well represented by the model.

As suggested by the above comparison of dip angles from models of different velocity structure, the shape of dip angle curve is sensitive to velocity structure. The observed curve does not fully coincide with the realistic Martigny 4 model, as would be expected, but in the northern part of the section is rather close to the high-velocity-contrast two-layer model Mar 3. This might be partly explained by the soil classification map existing for this area (FOEN 2013), which shows soil class D (V_s30 in the range 150–300 m s^{-1}) dominating in the northern part of the section, and soil C (V_s30 in the range 300–500 m s^{-1}) dominating in the southern part of the section. Moreover, the thickness of the glaciolacustrine deposits is increasing from south to north (Fig. 3).

8 DISCUSSION

Resonance frequencies for SH_{00}, SH_{01} and SV_0 obtained with FDD compare very well with published resonance frequencies from Roten *et al.* (2006) and Roten & Fäh (2007), with a deviation of less than 5 per cent. Mode shapes were previously obtained from measurements at Vétroz using site-to-reference spectral ratio. Comparison of our (arbitrarily scaled) FDD results to these mode shapes also yields good agreement (compare Fig. 14).

Sensitivity of the mode shapes and dip angles could be assessed in a qualitative way. Both *SH* fundamental mode shape and SV_0 dip angles show sensitivity to valley shape. Sensitivity of the dip angles of SV_0 to bedrock shape is quite pronounced, but decreases with the introduction of realistic layering in the model. Valley shape appears to control the zero crossing and edge values of the dip angle curve. Since this observation is based on one set of models only (models 7–10), further work is necessary to strengthen this conclusion. Observed dip angles at Martigny agree well with the zero crossing and edge values of the models, indicating a realistic valley shape has been employed. On the other hand, the shape of the curve, which we found to be influenced by velocity structure, is in approximate, but not good agreement with the layered velocity structure from reflection seismics and inversion of surface wave dispersion curves. Variability of the soil conditions along the profile might explain part of these differences. Moreover, the uncertainty on dip angle values is still considerable. A more precise measurement of dip values is therefore necessary to resolve this issue.

The six-layer model proved very valuable for the interpretation of observations at Martigny. Modelled and observed mode shapes fit very well in the *P–SV* case. It was, however, observed that variations of bedrock shape, velocity structure and Poisson ratio influence resonance frequencies, mode shapes and the sequence of modes considerably. Therefore, the results from Martigny cannot be extended easily to other locations, but more detailed modelling of each location would be necessary to assess their mode sequences.

Table 3 suggests that several modes with nodes in vertical direction have been found at Martigny. However, vertical nodes are only suggested on the basis of modelling. For the *SH* case, a homogeneous model had to be used. Analogue to the *P–SV* case, we argue that a layered model would show mostly higher modes that are focused in the upper layers and do not contain nodes in vertical direction. No indication was found that the observed *SH* modes are modes with vertical nodes. This is why in Table 1 all *SH* modes are listed as SH_{0x} modes.

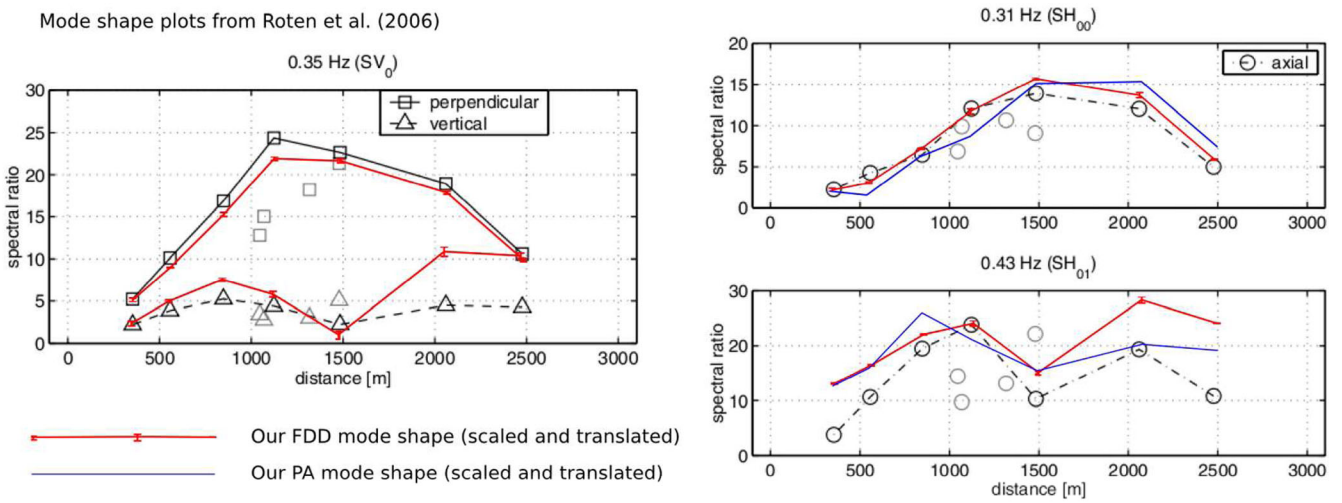

Figure 14. Comparison of arbitrarily scaled mode shapes obtained in this study and by Roten *et al.* (2006).

In the *P–SV* case a node in vertical direction on at least one of the two components is predicted for almost all modes. However, for all of these modes except the one at 0.55 Hz, nodes in depth are a result of our very strict definition that every zero crossing is a node, even if effectively motion occurs only on one side of the node, while on the other, close-to-zero motion is seen. The mode observed at 0.55 Hz, modelled at 0.52 Hz, remains the only observed mode with a modelled node in vertical direction that shows significant motion on either side of the node. Since its perpendicular component, the component containing this node, could not be observed, we deduce that resonance motion containing nodes in the vertical direction is not excited to observable amplitudes by the incident ambient vibration wavefield in the Rhône valley.

The fundamental *P* mode was not observed. We suggest that it is indeed not part of the modal sequence of the cross-sections studied here. BB85 obtained a critical shape ratio of 0.5–0.6 for the P_0 mode, using a model with a bedrock–sediment velocity contrast of 5:1. Although they did not provide an explicit formula for the critical shape ratio of *P* modes, with the velocity contrast of approximately 3:1 of our study area, the critical shape ratio may not be reached in the studied cross-sections. Moreover, sediment Poisson ratio at Martigny may be too high for this mode to occur (between 0.4 and 0.48), as with a high Poisson ratio the P_0 mode is no longer part of the modal sequence (suggested by model Mar 4).

9 CONCLUSION

We obtained good agreement of the resonance frequencies identified here with published results. Good agreement was also found between the two methods FDD and PA, and between observed and modelled results. Therefore, we are confident about the previously unmeasured frequencies and mode shapes. The frequencies recorded in Table 1 present a new extensive compilation of resonance frequencies of the Rhône valley sediment fill, which may be of use to further studies. The 'breathing' P_0 mode could not be observed and we propose that it is not part of the modal sequence of the Rhône valley. Excitation of modes with nodes in vertical direction is too low for these modes to be observed with our present data and processing techniques.

Observations from PA can potentially be obtained using only a single station or a small number of stations. Although we did not test this possibility, the relatively stable results from two array measurements at Sion indicate it is feasible. To test this approach, and to develop a more reliable identification for the dip angle from PA, is a subject for further research.

Observations and numerical modelling of the mode shapes fit very well down to details in the case of section Martigny, as was shown in Fig. 13. While the homogeneous model fails to reconstruct certain details, they are well reproduced by the realistic six-layer model. Thus, mode shapes apparently carry valuable information on the properties of the different layers. This is underlined by other observations, such as the coincidence of maximum of the mode shape with the extent of glaciolacustrine sediments in the case of section Bramois. It is a subject of further studies if and how this information can be conveniently used. Our modelling efforts have illustrated two important difficulties that have to be addressed here: The first is that the sequence of modes as they appear by frequency depends strongly on the subsurface properties. Therefore, observed modes have to be interpreted carefully. The second is the ambiguity concerning bedrock interface shape and velocity structure. For example, a symmetric mode shape may be related either to a symmetric valley shape or it might develop due to a significant velocity contrast at a layer boundary. Therefore, it may only be possible to extract information from resonance observations by including prior information on subsurface properties, similar to how it was done in the inversion study performed by Roten & Fäh (2007).

ACKNOWLEDGEMENTS

We would like to acknowledge the contribution of Daniel Roten who has made the array data from previous studies available to us. We also thank Clotaire Michel for his help with fieldwork and valuable advice on the use of the FDD processing method.

Wavelet software used in the PA was provided by C. Torrence and G. Compo, available at http://paos.colorado.edu/research/wavelets/. The Reform code for approximating 2-D resonance frequencies was kindly provided by Roberto Paolucci. Several figures in this paper were made using Generic Mapping Tools (GMT) 4 by Wessel & Smith (1998).

REFERENCES

Aki, K. & Richards, P.G., 1980. *Quantitative Seismology,* Vol. 1424, Freeman.

Bard, P.Y. & Bouchon, M., 1985. The two-dimensional resonance of sediment-filled valleys, *Bull. seism. Soc. Am.,* **75**(2), 519–541.

Bonnefoy-Claudet, S., Cotton, F. & Bard, P.Y., 2006. The nature of noise wavefield and its applications for site effects studies: a literature review, *Earth Sci. Rev.,* **79**(3), 205–227.

Brincker, R., Zhang, L. & Andersen, P., 2001. Modal identification of output-only systems using frequency domain decomposition, *Smart Mater. Struct.,* **10**(3), 441–445.

Burjánek, J., Gassner-Stamm, G., Poggi, V., Moore, J.R. & Fäh, D., 2010. Ambient vibration analysis of an unstable mountain slope, *Geophys. J. Int.,* **180**(2), 820–828.

Burjánek, J., Moore, J.R., Molina, Y., Freddy, X. & Fäh, D., 2012. Instrumental evidence of normal mode rock slope vibration, *Geophys. J. Int.,* **188**(2), 559–569.

Cerveny, V., 2005. *Seismic Ray Theory*, Cambridge Univ. Press.

Fäh, D., Suhadolc, P. & Panza, G.F., 1994. A hybrid method for the estimation of ground motion in sedimentary basins: quantitative modelling for Mexico City, *Bull. seism. Soc. Am.,* **84**(2), 383–399.

Field, E.H., 1996. Spectral amplification in a sediment-filled valley exhibiting clear basin-edge-induced waves, *Bull. seism. Soc. Am.,* **86**(4), 991–1005.

Field, E.H., Hough, S.E. & Jacob, K.H., 1990. Using microtremors to assess potential earthquake site response: a case study in Flushing Meadows, New York City, *Bull. seism. Soc. Am.,* **80**(6A), 1456–1480.

FOEN, 2013. Federal Office for the Environment: Web-GIS of the Office for Environment, Earthquakes subsoil classes. Available at: http://map.bafu.admin.ch (last accessed 14 August 2013).

Frischknecht, C. & Wagner, J.J., 2004. Seismic soil effect in an embanked deep alpine valley: a numerical investigation of two-dimensional resonance, *Bull. seism. Soc. Am.,* **94**(1), 171–186.

Guéguen, P., Cornou, C., Garambois, S. & Banton, J., 2007. On the limitation of the H/V spectral ratio using seismic noise as an exploration tool: application to the Grenoble valley (France), a small apex ratio basin, *Pure appl. Geophys.,* **164**(1), 115–134.

Havenith, H.B., Fäh, D., Alvarez-Rubio, S. & Roten, D., 2009. Response spectra for the deep sediment-filled Rhône Valley in the Swiss Alps, *Soil Dyn. Earthq. Eng.,* **29**(1), 17–38.

King, J.L. & Tucker, B.E., 1984. Observed variations of earthquake motion across a sediment-filled valley, *Bull. seism. Soc. Am.,* **74**(1), 137–151.

Le Roux, O., Cornou, C., Jongmans, D. & Schwartz, S., 2012. 1-D and 2-D resonances in an Alpine valley identified from ambient noise measurements and 3-D modelling, *Geophys. J. Int.,* **191**(2), 579–590.

Michel, C., Guéguen, P., El Arem, S., Mazars, J. & Kotronis, P., 2010. Full-scale dynamic response of an RC building under weak seismic motions using earthquake recordings, ambient vibrations and modelling, *Earthq. Eng. Struct. Dyn.,* **39**(4), 419–441.

Moczo, P., Labák, P., Kristek, J. & Hron, F., 1996. Amplification and differential motion due to an antiplane 2D resonance in the sediment valleys embedded in a layer over the half-space, *Bull. seism. Soc. Am.,* **86**(5), 1434–1446.

Paolucci, R., 1999. Shear resonance frequencies of alluvial valleys by Rayleigh's method, *Earthq. Spectra,* **15**(3), 503–521.

Pfiffner, O.A., Heitzmann, P. & Frei, W., 1997. *Deep Structure of the Swiss Alps: Results of NRP 20*, Birkhäuser.

Rial, J.A., 1989. Seismic wave resonances in 3-D sedimentary basins, *Geophys. J. Int.,* **99**(1), 81–90.

Roten, D. & Fäh, D., 2007. A combined inversion of Rayleigh wave dispersion and 2-D resonance frequencies, *Geophys. J. Int.,* **168**(3), 1261–1275.

Roten, D., Fäh, D., Cornou, C. & Giardini, D., 2006. Two-dimensional resonances in Alpine valleys identified from ambient vibration wavefields, *Geophys. J. Int.,* **165**(3), 889–905.

Roten, D., Fäh, D., Olsen, K.B. & Giardini, D., 2008. A comparison of observed and simulated site response in the Rhône valley, *Geophys. J. Int.,* **173**(3), 958–978.

Steimen, S., Fäh, D., Kind, F., Schmid, C. & Giardini, D., 2003. Identifying 2D resonance in microtremor wave fields, *Bull. seism. Soc. Am.,* **93**(2), 583–599.

Trifunac, M.D., 1971. Surface motion of a semi-cylindrical alluvial valley for incident plane SH waves, *Bull. seism. Soc. Am.,* **61**(6), 1755–1770.

Vidale, J.E., 1986. Complex polarization analysis of particle motion, *Bull. seism. Soc. Am.,* **76**(5), 1393–1405.

Wessel, P. & Smith, W.H.F., 1998. New, improved version of the Generic Mapping Tools released, *EOS, Trans. Am. geophys. Un.,* **79,** 579.

Wirgin, A., 1995. Resonant response of a soft semi-circular cylindrical basin to an SH seismic wave, *Bull. seism. Soc. Am.,* **85**(1), 285–299.

Yeh, C.S., Teng, T.J. & Chai, J.F., 1998. On the resonance of a two-dimensional alluvial valley, *Geophys. J. Int.,* **134**(3), 787–808.